Proceedings of the
Annual Stability Conference
Structural Stability Research Council
Louisville, Kentucky, April 13-16, 2021

Design of orthotropic steel diaphragms for improved building stability through topology optimization

Astrid W. Fischer[1], Federico Ferrari[2], James K. Guest[3], Benjamin W. Schafer[4]

Abstract

For buildings subjected to earthquake actions, it is critical that floor and roof diaphragms can guarantee an overall behavior to the structure, transferring the loads to the vertical lateral force resisting systems and enhancing the global stability. Recently, the authors have applied topology optimization to steel deck diaphragm designs considering a linearly elastic response. By optimizing the deck selection and orientation novel, constructable, diaphragm designs with high stiffness were achieved. In this work, the elasto-plastic response of traditional and optimized diaphragms is compared to these designs, both in terms of ultimate bearing capacity and energy dissipation. It is found that the optimized decks have superior performance to typical deck designs even if they were optimized with respect to linear stiffness alone. These findings will promote further research of the design of novel diaphragm deck configurations, that are both stiffer and more stable even under plastic deformations. This work is part of a larger initiative (steeli.org) that aims to better understand and optimize the role of diaphragms in the seismic response of steel buildings.

1. Introduction

The diaphragm's role in an effective building design is changing, new design methods and research suggest that diaphragms regularly experience inelastic seismic demands and that diaphragm force levels are greater than specified. In addition, a surge in new shapes of buildings with unique floor plans, require diaphragms with complex shapes that can support cutouts and openings. The demand for efficient, sustainable, and resilient building designs drives the potential rethinking and innovation for new and efficient systems. Seismic design of buildings relies on both the vertical and horizontal lateral force resisting systems (LFRS), where the purpose of the vLFRS is to transfer the lateral load to the ground, while the hLFRS, e.g., the diaphragm, is responsible for distributing the large inertia forces originating from the mass on the floors and resist the gravity demands of this mass. Successful seismic design may employ the diaphragm to take multiple roles such as, but not limited to, providing lateral support to the vLFRS and redistribution of forces due to openings, as summarized in Easterling, et al. (2018).

[1] Graduate Research Assistant, Johns Hopkins University, winther@jhu.edu
[2] Postdoctoral Fellow, Johns Hopkins University, fferrar3@jhu.edu
[3] Associate Professor, Johns Hopkins University, jkguest@jhu.edu
[4] Professor, Johns Hopkins University, schafer@jhu.edu

A large study of 3D steel-framed building archetypes has been performed to study the seismic performance of elastic and inelastic designed steel deck diaphragms, one example is illustrated in Figure 1 (Foroughi, et al., 2021). A common choice for floor and roof diaphragms is the bare and composite steel deck diaphragms, respectively, and for which examples are shown in Figure 2. In this paper, these archetype buildings provide baseline geometric properties for a typical diaphragm design.

Topology Optimization (Bendsøe & Sigmund, 2004) is nowadays a well-established, valuable tool for the conceptual definition of innovative designs. The method has been extensively applied to a wide variety of engineering fields, with application in mechanical, aeronautical, robotics, material design, design for fluids, etc. the reader is referred to (Sigmund & Maute, 2013) for a survey on topology optimization methods and (Deaton & Grandhi, 2014), (Osanov M., 2016) for recent applications. When compared to the above-mentioned fields, the use of topology optimization for civil engineering applications seems to be lagging behind. This might be due to the following two reasons, considerably reducing the design freedom:

1. Civil engineering structures are usually subjected to different loads and actions and have various requirements and standards to comply with. This is not easy to model in an optimization framework
2. Optimized designs usually are intricate and this introduces heavy challenges for their practical realization.

Concerning the last point, (Fischer, et al., 2020) have successfully used topology optimization to find novel diaphragm designs for several floor/roof plans and, upon a post processing of the optimized design, achieved a deck design that is practically constructable. With a number of configurations which provide an almost continuous design space for strength and stiffness of available decks. Additionally, a steel deck diaphragm is composed of many individual decks that potentially can be any deck type and attached at any orientation. This provides optimization on both the deck type i.e., the strength and stiffness, the attachment detail, and the orientation of each deck segment.

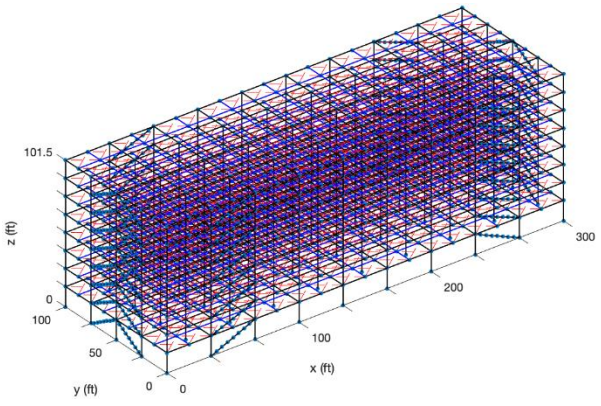

Figure 1: Isometric elevation of SDII building archetype with CBF braced frames (Foroughi, et al., 2021).

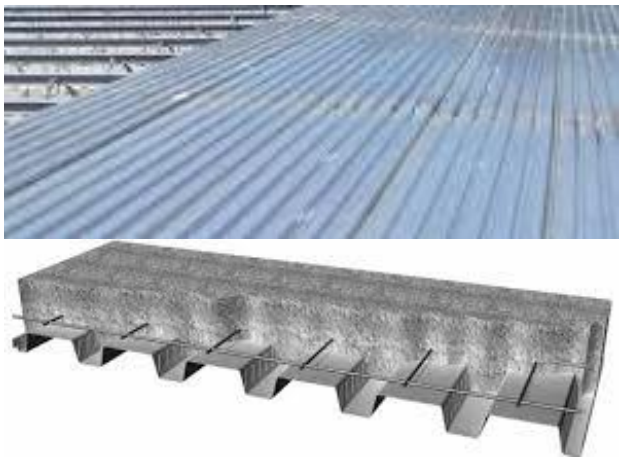

Figure 2: Steel deck diaphragms (top) roof - bare deck on open web steel joists (ASC, 2018), (bottom) floor - concrete filled deck (ASC, 2018)

The investigation in Fischer, et al. (2020) was limited to linear compliance minimization. Here the nonlinear response will be extended, by investigating the ability of the innovative designs of (Fischer, et al., 2020) to withstand elasto-plastic deformation, comparing their performance to that of "traditional" designs. This is clearly an important feature for a diaphragm, measuring its ability to absorb plastic deformations and thus to dissipate the energy introduced by a seismic event.

In this paper, the optimized decks obtained by (Fischer, et al., 2020) are compared to the more "classical" designs (widely used in common engineering practice), by performing a pushover analysis, assuming the plasticization is affecting the shear resistance of the deck. Using the material properties of steel deck diaphragms, with an orthotropic material model capturing the diaphragm deck behavior observed in (Schafer, et al., 2018), the decks' performances will be compared.

The remainder of the paper is organized as follows: Section 2 overviews the main analysis tools and introduces the diaphragm examples discussed. In Section 3 the different designs are compared based on a simple elastic analysis, whereas the nonlinear, pushover analysis is performed in Section 4. Finally, Section 5 gives some final discussion and a perspective on future works.

2. Setup and methods

2.1 Equivalent Stiffness and Strength Properties of Steel Deck Diaphragms

A bare steel deck diaphragm is composed of several units, called "decks", that are connected along the edges by sidelap fasteners, and connected to the underlying structure by structural fasteners. The strength and stiffness of the diaphragm are influenced by the number and type of sidelap and structural fasteners, by the spacing of the underlying substructure, and by the thickness and corrugation layouts of the steel deck itself. Steel deck diaphragms are designed for shear strength and stiffness according to AISI S310 (AISI, 2013), where formulas developed for corrugated steel decks are specified. The axial stiffnesses of the bare steel decks both along and across the corrugations are estimated with Xia and Friswell's method for highly orthotropic corrugated plates (Xia & Friswell, 2012).

Extensive strength tables developed per AISI S310 are provided in DDM04 (Luttrell, 2015), covering over 65,000 configurations of bare steel decks for use in design. Based on this source, equivalent shear strength V , shear stiffness G', and the axial stiffnesses in the directions parallel and perpendicular to the corrugations, E_1' and E_2', are estimated for the diaphragm decks. The prime symbol remarks that these latter are equivalent material moduli representing the plate stiffnesses; thus, they account for the thickness of the deck ($G' = G\ t$).

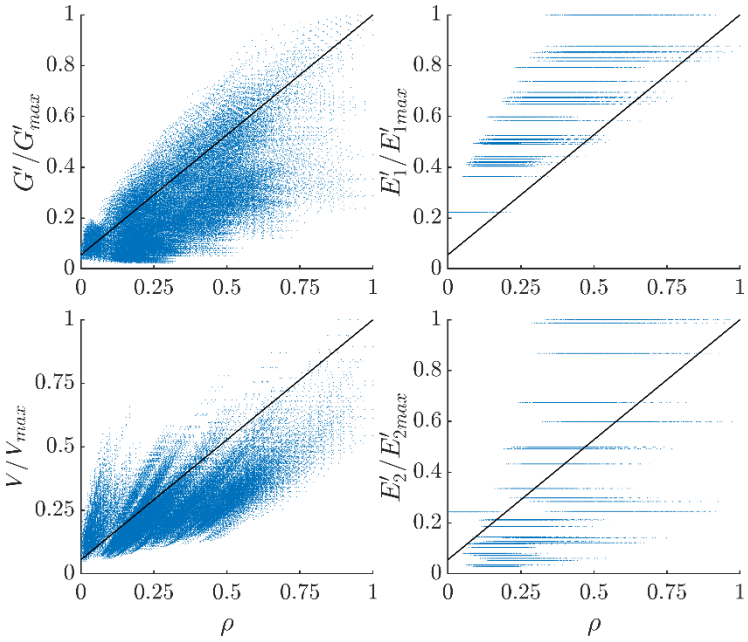

Figure 3: Shear stiffness, axial stiffnesses and shear strength variation with design variable ρ.

Table 1: Equivalent moduli and shear strength of bare steel decks.

Property	US units	SI units
$E_{1_{max}}'$	2885 kips/in	505,200 kN/m
$E_{2_{max}}'$	0.8947 kips/in	156.7kN/m
G'_{max}	241.1 kips/in	942.1 kN/m
V_{max}	4995 lb/ft	3389 N/m

Table 2: Elasto-plastic model properties for the bare steel decks.

γ_u	4%
τ_Y	$0.8\,V$
γ_Y	τ_Y/G'
G_t'	$\frac{0.2\,V}{\gamma_u - \gamma_Y}$

Linear approximations of the strength and stiffnesses are realized as a function of the variable ϱ and illustrated in Figure 3, where liner interpolation for any of strength and stiffness properties, say "$(\cdot)$" can be achieved with:

$$(\cdot)(\varrho) = \frac{\varrho}{\varrho_{max}}\,(\cdot)_{max} \tag{1}$$

where G'_{max}, V_{max}, $E'_{1,max}$ and E'_{max} are listed in Table 1. The variable ϱ is a function of the corrugation length over corrugation width (s/d), plate thickness (t), strength of the structural and sidelap fasteners (P_{nf}, P_{ns}) and spacing (L) of these connections:

$$\varrho = \frac{s}{d}\frac{t}{t_{max}}\left(\frac{L_{max}}{L}\frac{P_{nf}}{P_{nf\,max}}\right)^{1/4}\left(\frac{L_{s\,max}}{L_s}\frac{P_{ns}}{P_{ns\,max}}\right)^{1/4} \tag{2}$$

For the designs discussed in the following, the selection of different decks in the diaphragm domain is performed through the continuous variable $\rho \in [0,1]$, defined as

$$\rho = \frac{\varrho - \varrho_{min}}{(\varrho_{max} - \varrho_{min})} \tag{3}$$

The shear strength and stiffness of the decks are a function of the sidelap and structural fasteners, though, the sidelap fasteners are often the weaker connection of the two and with a continuous shear load on the deck, shear tearing and bearing of the deck against the fastener or fracture of the deck around a weld can occur (Torabian, et al., 2018). This bearing failure of the sidelap connections will impact the shear stiffness of the deck, while the axial stiffness parallel to the corrugations (E_1) will reduce slightly, assuming the lower flange that the sidelap connections are made into are no longer effective parts of the deck corrugations. This reduction in axial stiffness

h

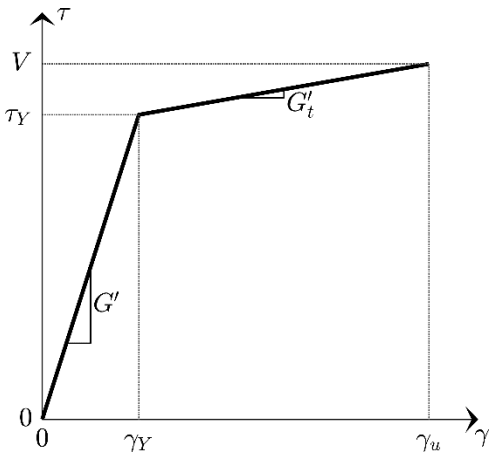

Figure 4: Bilinear (shear) stress-strain realtionship used for the elastoplastic modeling.

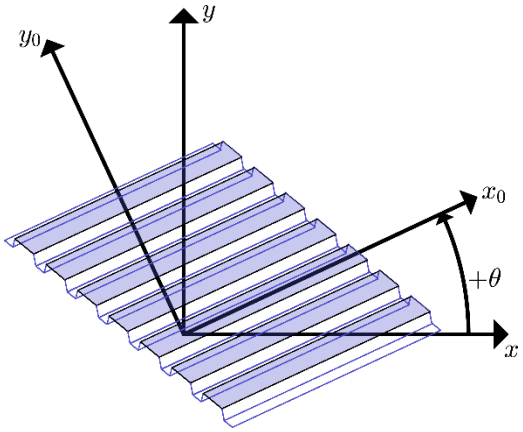

Figure 5: Global coordinate system, oriented along the diasphragm's directions (x, y), and local coordinate system, orinted along the principal directions of orthotropy (x_0, y_0).

is between 0.1-16.7% for bare steel decks, but will not be considered in this analysis. As long as the structural fasteners are still effective, the deck is still attached to the underlying structure, however, the structural connections will begin to detach from the deck at a shear angle of approximately 4%, where the deck is considered to fail. Based on this reasoning, the nonlinear model assumes that the plasticization of the deck is governed by shear deformations and by reducing the shear stiffness alone.

The plastic formulation will be written in the local material system, where (τ_0, γ_0) is the only work-conjugate pair in the plastic potential, and they are decoupled from the other stress/strain terms in the local material system, essentially having a 1D plasticity problem (Borja, 2013). The yielding function becomes:

$$\psi = |\tau_0| - \tau_Y \tag{4}$$

where $\tau_Y(\rho_e)$ is the yielding shear stress, based on the deck's shear strength $V(\rho_e)$. The yielding stress is set to $\tau_Y(\rho_e) = 0.8\,V(\rho_e)$, and together with the ultimate and yielding shear angle ($\gamma_u = 0.04$, $\gamma_Y(\rho_e) = (\tau_Y/G')(\rho_e)$), this completely defines the bilinear curve governing the elasto-plastic response. The tangent (G'_t) and yielding (H') moduli are then defined as:

$$G'_t(\rho_e) = \frac{0.2\,V(\rho_e)}{\gamma_u - \gamma_Y(\rho_e)}, \quad H'(\rho_e) = \frac{G'_t(\rho_e)}{1 - G'_t(\rho_e)/G'} \tag{5}$$

2.2 Discretization and Governing Equations

The analyses in the following are performed by discretizing the diaphragm's domains Ω by a structured grid of equi-sized Q_4 finite elements, each one denoted as Ω_e. The elemental elasticity matrix in the local material system is (Jones, 1999):

$$\boldsymbol{D}_0^e(\rho_e) = \frac{1}{1 - \nu_{12}\nu_{21}(\rho_e)} \begin{pmatrix} E'_{11}(\rho_e) & \nu_{12}E'_{22}(\rho_e) & 0 \\ \nu_{21}E'_{11}(\rho_e) & E'_{22}(\rho_e) & 0 \\ 0 & 0 & G'(\rho_e) \end{pmatrix} \tag{6}$$

where the material moduli are obtained by interpolation, and ν_{12}, ν_{21} are the Poisson's coefficients. In the following $\nu_{12} = 0.35$ is fixed, whereas $\nu_{21}(\rho_e) = \nu_{12}E'_{22}/E'_{11}$ v depends on the interpolation variable. The elasticity matrix is referred to the global coordinate system through the relationship:

$$\boldsymbol{D}^e(\rho_e, \theta_e) = \boldsymbol{R}^e(\theta_e)\boldsymbol{D}_0^e(\rho_e, \theta_e)[\boldsymbol{R}^e(\theta_e)]^T \tag{7}$$

where $\boldsymbol{R}^e(\theta_e)$ is the orthogonal rotation matrix for plane tensors. The elemental stiffness matrix then reads:

$$\boldsymbol{K}^e(\rho_e, \theta_e) = \int_{\Omega_e} \boldsymbol{B}^T \boldsymbol{D}^e(\rho_e, \theta_e)\boldsymbol{B}\ d\Omega_e \tag{8}$$

where $\boldsymbol{B}$ is discretizing the strain-displacement operator. The assembly of each elemental contribution (8) into the global stiffness matrix, and the assembly of the vector of external forces ($\boldsymbol{F}_{ext}$) gives the algebraic system $\boldsymbol{K}\boldsymbol{u} = \boldsymbol{F}_{ext}$, that is the solved for the linearized equilibrium displacement $\boldsymbol{u}$.

With $\boldsymbol{u}$ in hand, the strains and stresses in the global reference system are computed through the relationships $\boldsymbol{\varepsilon} = \{\varepsilon_x, \varepsilon_y, \gamma\}^t = \boldsymbol{B}\boldsymbol{u}$ and $\boldsymbol{\sigma} = \{\sigma_x, \sigma_y, \tau\}^t = \boldsymbol{D}^e(\rho_e, \theta_e)\boldsymbol{\varepsilon}$, respectively. Then, the quantities in the local material system are recovered as $\boldsymbol{\varepsilon}_0 = \boldsymbol{R}^e(\theta_e)\boldsymbol{\varepsilon}$, and $\boldsymbol{\sigma}_0 = \boldsymbol{R}^e(\theta_e)\boldsymbol{\sigma}$.

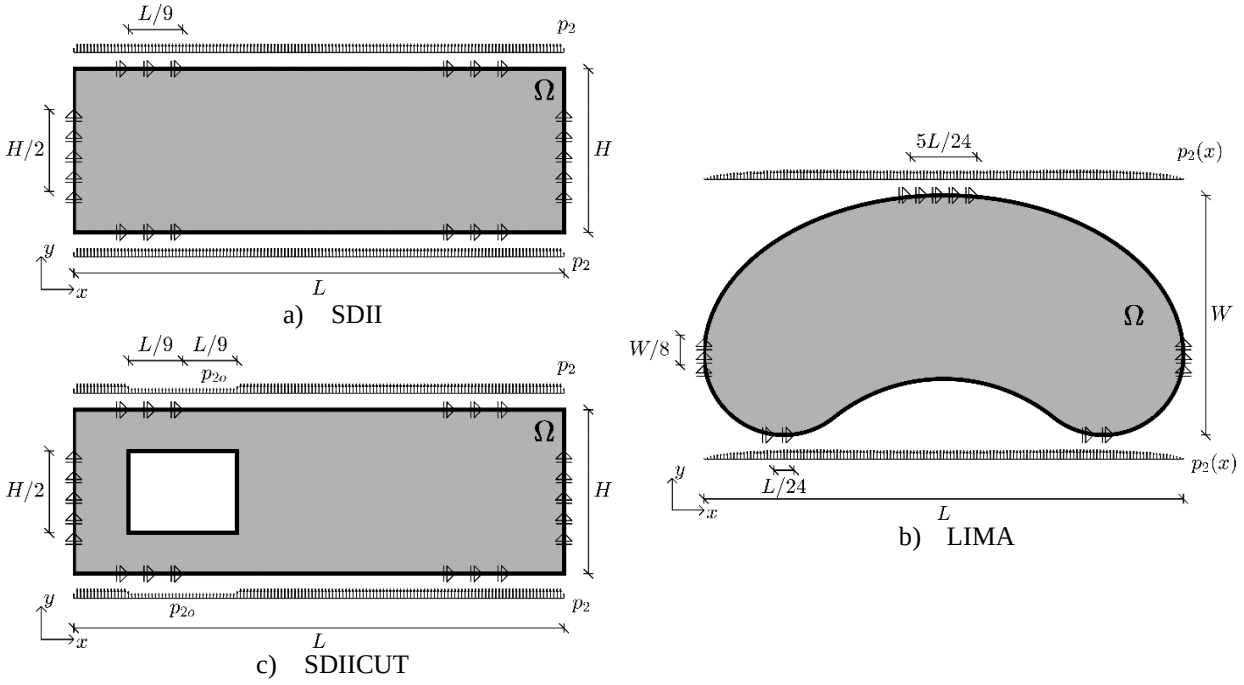

Figure 6: Geometry, loadings and boundary conditions of the diapharagm examples considered. (a) standard diaphragm for the SDII archetype building model (Foroughi, et al., 2021), (b) SDII diaphragm with a cutout, (c) organic shaped diaphragm. The constraints on the perimeter are rollers restraining the horizontal/vertical relative displacements at locations where the bracing systems connect to the diaphragm. Numerical values for the geometric dimensions and loads are summarized in

.

Table 3: Geometrical dimensions and data for the diaphragms examples

Property	US units	SI units
L – length	300 ft	91.44 m
H – height	100 ft	30.48 m
W – width	150 ft	45.72 m
F_{px} (SDII)	262 kips	1165 kN
F_{px} (SDIICUT)	245 kips	1090 kN
F_{px} $(LIMA)$	285 kips	1266 kN

2.3 Diaphragm Design Layouts

The setups for the diaphragm example considered in the following are shown in Figure 6, and the dimensions and load values are reported in Table 3. The rectangular diaphragms in Figure 6(a) and (b), hereafter called *SDII* and *SDIICUT*, are inspired by the SDII archetype building model (Torabian, et al., 2017). The *LIMA* configuration in Figure 6(c) is inspired by the DC Water headquarter building in Washington D.C. (Grant & Stewart, March 2018).

For all the configurations, displacement boundary conditions represent the effect of the vLFRS connected to the diaphragm. The vLFRS can only offer significant resisting forces in their plane (see Figure 3), while they basically do not resist out-of-plane forces. Therefore, the boundary conditions are modeled as rollers, restraining the relative vertical (viz., horizontal) displacements along the edges.

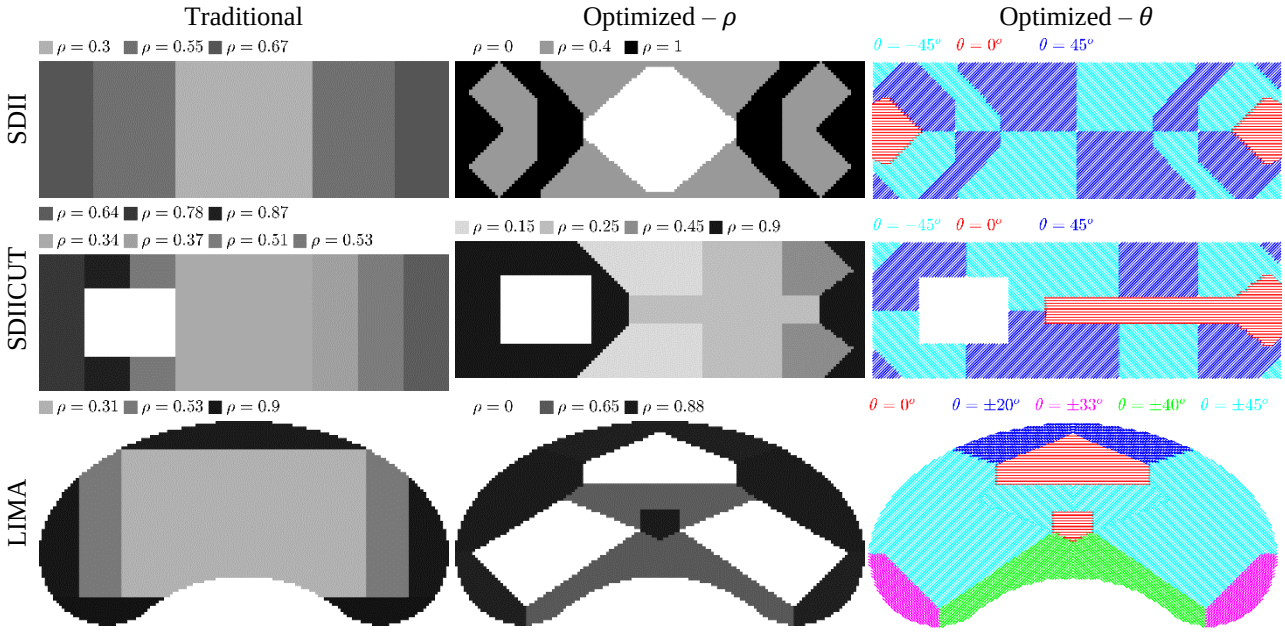

Figure 7: Comparison of the traditional (leftmost column) and compliance optimized and post-processed (center and rightmost columns) layouts. The grayscale reflects the distribution of the selector ρ, thus the variation of stiffness and strength (mean(ρ) $\approx$ 0.5 is maintained for all the designs). Colored lines indicate different orientations (θ) of the strong material axis. The traditional designs have $\theta = 0$.

A uniform weight distribution across the floor is assumed, and the magnitude of the load applied to each diaphragm is proportional to its area. In this way, the total force, applied in the y direction F_{px}, equals the seismic diaphragm design force according to ASCE 7 (ASCE 7-16, 2016) for the SDII archetype building (Torabian, et al., 2017), and equal mass proportions for the SDIICUT and LIMA (see Table 3).

Figure 7 shows the distribution of the material selector ρ_e and the orientation of the strong axis θ_e for two diaphragm designs. Designs in the left column will be referred to as "traditional" in the following, whereas the designs in the other 2 columns will be called "optimized". These latter were obtained through a manual post processing of the optimized designs resulting from topology optimization (Fischer, et al., 2020), (Fischer, et al., 2019). Indeed, the raw designs given by the topology optimization show rapidly varying orientations and a continuous orientation of the ρ parameters, features that are clearly against the practical construction of these designs. The post processing operation was applied to extract a few macro-regions with uniform, discrete values of ρ and θ, thus making the design potential in construction. However, it is clear from Figure 7 that the post-processing operation also introduces discontinuities in the deck's layout. This will later be shown to have a detrimental effect in the deck's response.

In the traditional designs the stiffness distribution follows the linearly varying shear demand along the beam span, given by an approximate calculation based on beam theory. Stiffer decks (dark areas) are selected at the ends, whereas the weaker deck types (light areas) are used at the midspan. Also, these traditional designs use a constant deck orientation $\theta = 0$ across the diaphragm, having the strong material axis perpendicular to the loading direction.

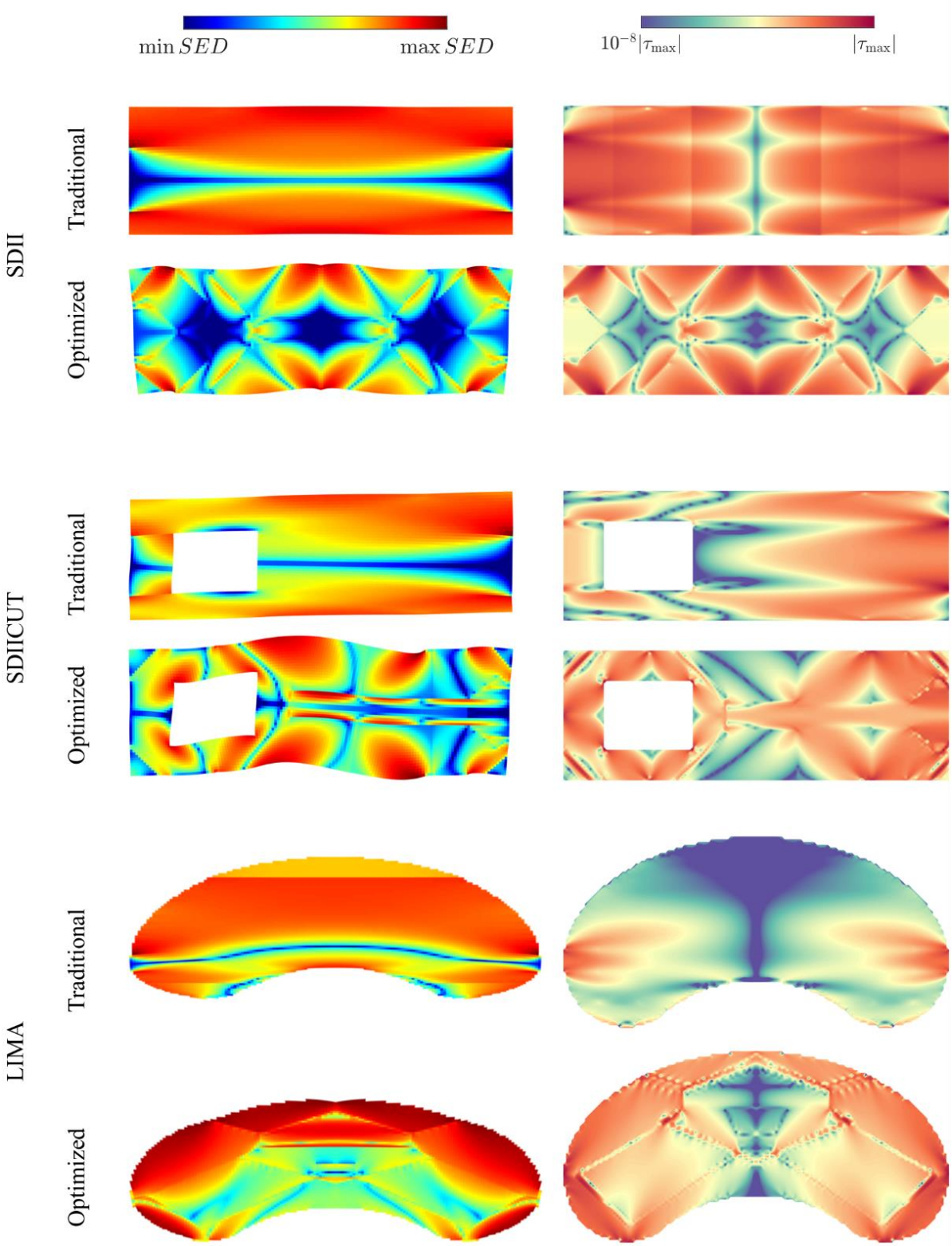

Figure 8: Elastic response of the traditional and optimized designs for the three diaphragm configurations. Plots on the left show the deformed configuration and the strain energy density (SED). Displacements are scaled by cUL_x, where c=0.01 and c=0.05 for the traditional and optimized designs, as the latter is much stiffer. Plots on the right show the local distribution of the shear stress.

3. Elastic Analysis of the Traditional and Optimized Designs

Before proceeding to the pushover response, it is useful to examine the elastic behavior of the different decks subjected to the external load with full magnitude ($|\boldsymbol{F}_{ext}|$). This will give useful information about the deformation and stress distributions for each design, and shows where the yielding will first take place. Results are provided in Figure 8, Figure 9 and Table 4.

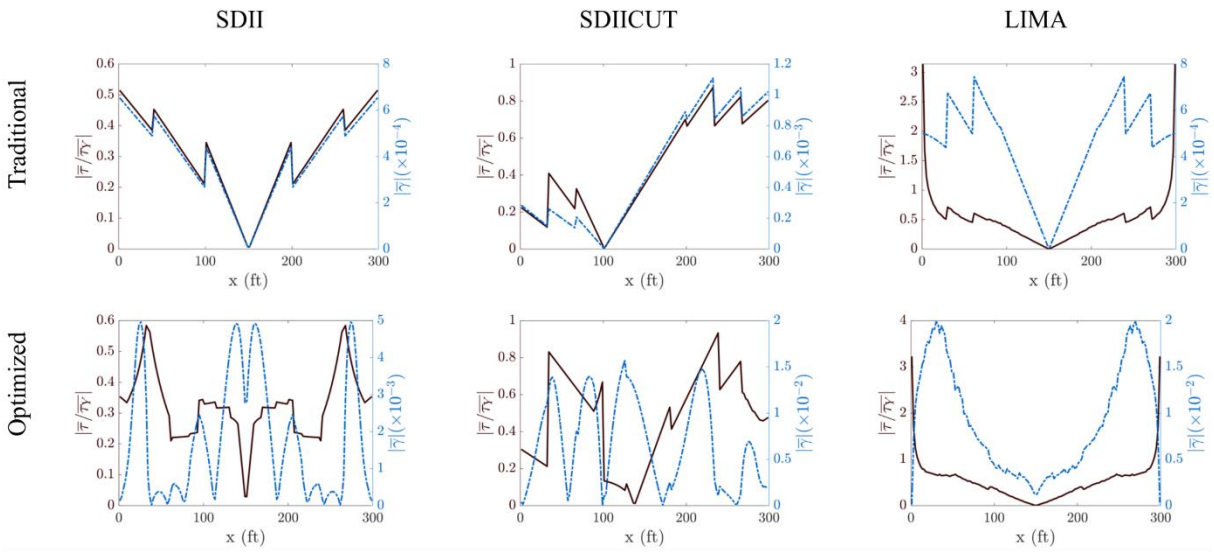

Figure 9: Mean values (i.e., averaged along the deck's depth) of the ratio between shear stress and yielding stress ($|\bar{\tau}/\overline{\tau_Y}|$, plotted agains the left axis) and of the shear strain ($|\bar{\gamma}|$, plotted against the right axis). These values are referred to decks responding *elastically* and to the load applied with full intensity.

The deformed configurations of the traditional and optimized decks are provided in the left column in Figure 8. All the traditional decks exhibit a deformation that is governed by the folding of the corrugation, where each horizontal fiber essentially responds individually, see plots in the left column of Figure 8, Traditional. Indeed, the traditional deck have a unidirectional behavior, because of the strong orthotropicity and the uniform horizontal orientation of the fibers. The optimized decks on the other hand, achieve an overall, beam-like deformation, due to the local fiber's varying orientation promoting the strong material axis E_{11}, and creating shear coupling. The superior deformation mechanism achieved by the optimized decks results in a much lower peak displacement, and lower compliance values (see Table 4 and the different scaling in the deformations of the traditional and optimized designs in Figure 8).

Colormaps in Figure 8 show the log-modulus scaled plot (i.e., $\text{sign}(y)\log_{10}(1+|y|/|y_{\max}|)$) of the strain energy density (SED) and of the shear stress. The stress plots give important information about which points in the design will yield first. The traditional designs systematically exhibit the highest stresses on the boundary, where the shear stress become larger than the yielding value (see Table 4). This is reasonable, even if the decks were designed according to the total load magnitude, as the calculation was based on a simplified beam model; thus, not capturing the local stress peaks introduced in the continuum by the boundary conditions. Moving away from these locations the stress is rapidly attenuated; therefore, traditional decks will be dominated by plastic behavior at the extreme sections. The stress distribution is more complex for the optimized decks, as now there are several locations of peak stress, some of them appearing away from the restrained locations.

This is due to the presence, in the optimized designs, of high gradients in stiffness, due to discontinuities in both ρ (deck and fastener choice) and θ (deck orientation) distributions.

Figure 8 shows the trend along the deck's span for the ratio between the shear stress and yielding stress ($|\bar{\tau}/\overline{\tau_Y}|$) and of the diaphragm shear angle ($\bar{\gamma}$). The overbar means that these quantities have been averaged over the deck's depth, so to have a one-dimensional distribution. For the traditional design, note the nearly linear shear distribution predicted by the 1D beam approximation within each region with constant strength. Generally, the "one-dimensional" averaged distribution shows peak values that are sensibly attenuated (compare Figure 9 and values in Table 4). This demonstrates the importance of local effects in the strength analysis of the decks.

Interestingly, the optimized decks show more peaks closer to each other, meaning that there are more points that will start to yield simultaneously. Also note, for the optimized designs, the regions with highest shear angle do not always coincide with the regions where the plasticization will happen first.

Table 4: Results from the elastic analysis of the diaphragm examples, for the traditional and optimized designs. Maximum displacement (u_{max}), external work (W), maximum shear stress (τ_{max}), maximum shear stress to yield stress (τ_{max}/τ_Y) and the maximum shear angle (γ_{max}).

		SDII		**SDIICUT**		**LIMA**	
		Optimized	**traditional**	**Optimized**	**traditional**	**Optimized**	**traditional**
u_{max}	[ft]	0.37	2.61	1.49	4.02	2.92	8.38
	[m]	*0.11*	*0.80*	*0.45*	*1.23*	*0.89*	*2.55*
W	[kips ft]	39.7	636.1	115.0	789.0	260.4	1308.3
	[kN m]	*53.9*	*862.5*	*155.9*	*1069.7*	*353.0*	*1773.8*
τ_{max}	[kips /ft]	35.3	15.6	69.5	25.5	47.1	41.5
	[kN/m]	*514.7*	*227.2*	*1014.3*	*372.5*	*687.6*	*605.8*
τ_{max}/τ_Y	[ ]	38.9	7.0	28.7	12.0	43.8	14.3
γ_{max}	[ ]	0.04	0.01	0.10	0.32	0.32	1.02

4. Pushover Analysis of the Traditional and Optimized Designs

"Pushover analysis" is performed by defining a load increment program $\boldsymbol{F}_{ext,k} = \lambda_k \boldsymbol{F}_{ext}$ through the multipliers $\boldsymbol{\lambda} = \{0, \lambda_1, \lambda_2, \dots, 1\}$. The load is exerted over 200 steps, thus λ_k=1/200, where each step uses Newton-Raphson method to solve the non-linear equilibrium equation:

$$\boldsymbol{r}(u_k) = \boldsymbol{F}_{int}(D_t, u_k) - \boldsymbol{F}_{ext,k} = \boldsymbol{0} \tag{9}$$

(see Section 2.2 and Appendix A for details). The diaphragm is considered to fail when the shear angle $\gamma_u = 4\%$ is reached. This value for the ultimate shear angle has been set according to building practice, as the shear deformation at which structural fasteners detach from the diaphragm.

The results of the analyses are summarized in Figure 10, Figure 11 and Table 5. The discussion will be based on the value of the load multiplier at yield and at failure (λ_Y,λ_u), the maximum shear angle at yield ($\gamma_{max,Y}$), and the maximum displacement at failure (u_{max}). Then, the evolution of the internal work ($\dot{\mathcal{W}}$) and of its purely plastic fraction ($\dot{\mathcal{W}}_p$) will be evaluated:

$$\dot{\mathcal{W}} = \int_\Omega \boldsymbol{\sigma}^t \, \dot{\boldsymbol{\varepsilon}} \, d\Omega \,, \quad \dot{\mathcal{W}}_p = \int_\Omega \dot{\gamma}_p \, \tau_Y \, d\Omega \tag{10}$$

where the latter is linked to the energy dissipated through damage.

For the SDII layout, the traditional design starts to yield in correspondence of the restrained regions on vertical edges (see Figure 10a), as predicted by the stress distribution in Figure 8. The traditional design shows a limited redistribution, as the plastic deformation γ_p (thus, the damage) remains localized in these regions and quickly increases up to the deck's failure. Overall, the traditional design develops first yield at $\lambda_Y = 0.15$ ($|\boldsymbol{F}_{ext}| = 38.0\ kips = 169.0\ kN$) and fails at $\lambda_u = 0.55$ ($|\boldsymbol{F}_{ext}| = 142.8\ kips = 635.2\ k$). On the other hand, the optimized design develops plasticity at the restrained locations on the horizontal edges and shows a much higher redistribution capacity. Figure 10b indicates how the pattern of how the pattern of plasticized regions extends over the interior of the diaphragm, propagating along the lines of high stiffness contrast. In particular, the interface between the stiffest regions and the low stiffness diamond, at the center of the domain (see Figure 7), is absorbing a lot of plastic deformation.

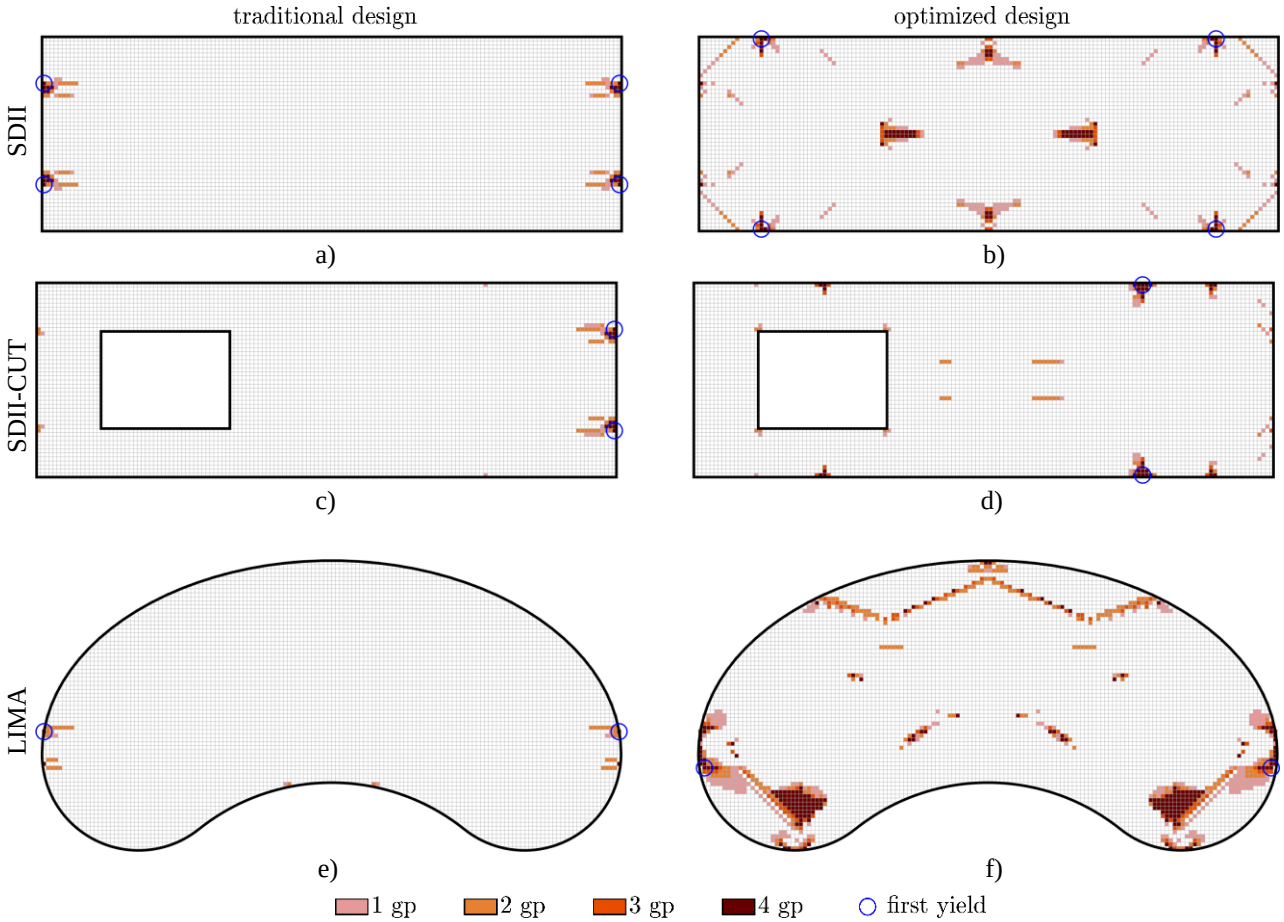

Figure 10: Plasticized regions at the failure stage for the traditional (left column) and optimized (right column) designs. The color distribution is according to the number of Gauss points within an element that are yielding and the circles indicates the location of initial yielding.

Concerning the strength, the optimized deck starts to yield early, with $\lambda_Y = 0.07$ ($|\boldsymbol{F}_{ext}| = 18.3\ kips = 81.4\ kN$). However, due to its ability to better redistribute stresses across the deck, it reaches the ultimate bearing capacity of $\lambda_u = 0.67$ ($|\boldsymbol{F}_{ext}| = 175.5\ kips = 780.8\ kN$), which is higher than the traditional design. Figure 11a illustrates the evolution of the work measures from Eq. 12 and of the maximum shear angle, as a function of the load increment λ. Note from the plots that:

1. The optimized deck is much stiffer than the traditional deck (has lower $\mathcal{W}$ values), for both the elastic and plastic ranges, see subplot a). This is expected for the elastic regime, but the deck was not explicitly optimized to consider the plastic response;
2. The optimized deck has a much better capability to dissipate energy compared to the traditional deck, as the ratio $\mathcal{W}_p/\mathcal{W}$ at failure is almost seven times higher than for the traditional deck;
3. The increase of the total shear angle γ, as yielding starts, is sudden for the traditional deck, and more gradual for the optimized one.

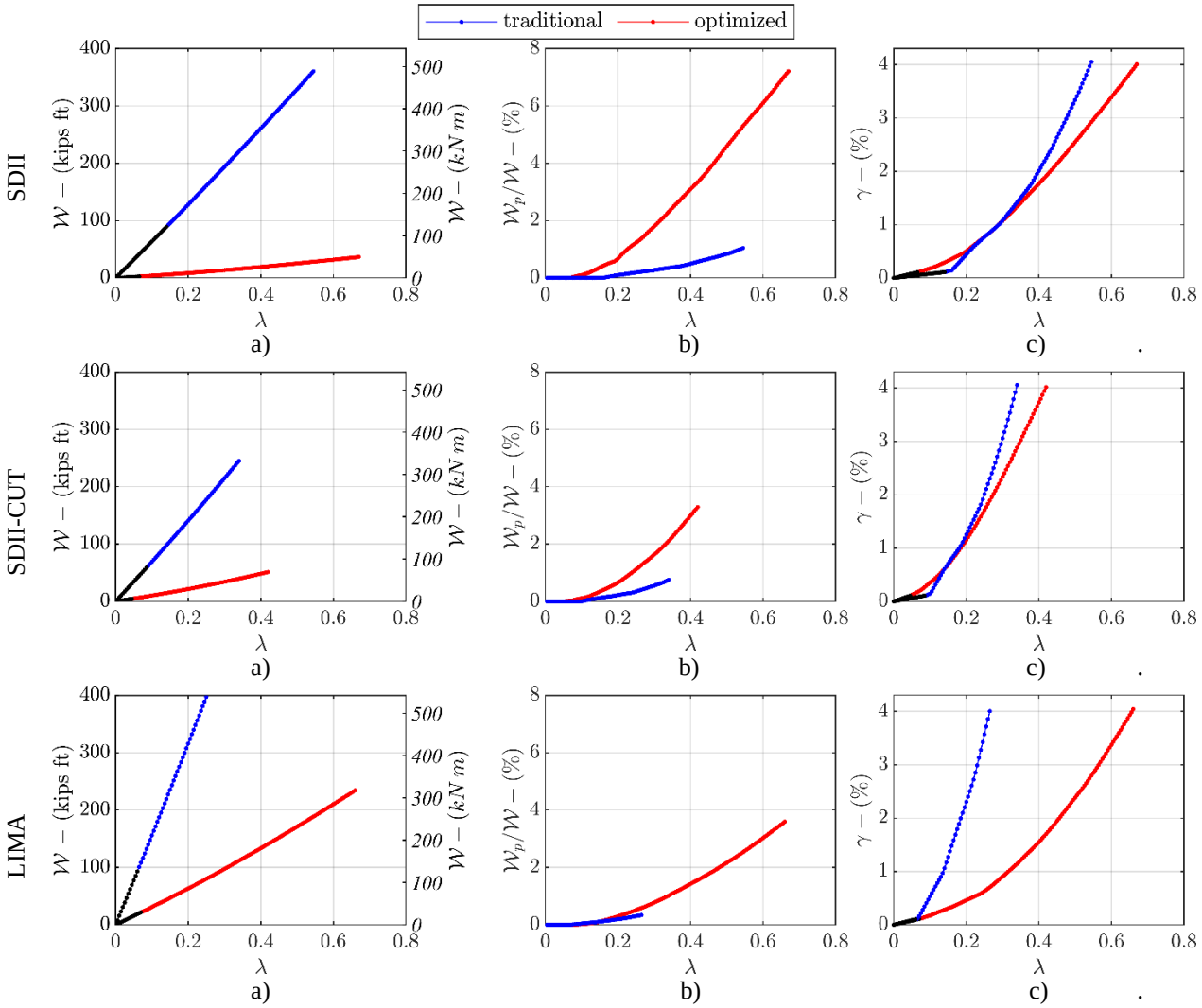

Figure 11: Pushover curves of the diaphragm examples for the traditional and optimized designs. Figures show the evolution oft he following quantities: a) total cumulative work, b) plastic work fraction of the total work, and c) maximum shear angle, as a function of the external load multiplier.

Concerning the SDIICUT and LIMA designs similar conclusions can be carried out, and relevant differences will be discussed. For the SDIICUT traditional design, yielding again occurs at the restrained boundary, first developing at the right edge (Figure 10c). In the SDIICUT optimized design yielding initializes at the horizontal boundary conditions, followed by yielding in the elements where deck type and orientations change and at the corners of the cutout, see Figure 10d. Again, the yielding starts much earlier for the optimized design than for the traditional design ($\lambda_Y = 0.05$ for the optimized design, versus $\lambda_Y = 0.09$ for the traditional design) and, for both cases, the ultimate load is now lower than that for the SDII deck. The traditional deck fails at $\lambda_u = 0.34$ and the optimized one at $\lambda_u = 0.42$.

For both LIMA designs the yielding initiates at the vertical restrained regions. For the optimized design the plasticized regions extend to the immediate area near all restrained boundaries and to interfaces where deck type and orientation change (see Figure 10f and Figure 7). High stress concentrations especially occur at a material change from $\rho = 0.88$ to $\rho = 0$, at the top of the diaphragm and the bottom of the diaphragm. Opposite the designs described above, both LIMA designs begin plasticizing at $\lambda_y = 0.07$, which also leads to the traditional design reaching the ultimate load before the optimized design: at $\lambda_u = 0.27$ and $\lambda_u = 0.66$

The plastic energy dissipated in the pushover is less than 1% of the total work for the 3 traditional designs, while the 3 optimized designs can dissipate energy between 3-7% of the total work. The optimized designs are in general performing better than the traditional designs, especially the LIMA optimized design, highlighting that even linear topology optimization can potentially give better designs for complex layouts and demands than traditional design.

Table 5: Results from the pushover analysis of the diaphragm examples, for the traditional and optimized designs. The load multiplier (λ), maximum shear angle (γ_{max}), and external work (W) are shown for the first yielding step, and at failure. At failure, maximum displacement (u_{max}) and relative amount of plastic work (W/W_p) are also shown.

			SDII		**SDIICUT**		**LIMA**	
			Optimized	**traditional**	**Optimized**	**traditional**	**Optimized**	**traditional**
first yield	$\boldsymbol{\lambda}$	[ ]	0.07	0.145	0.050	0.09	0.075	0.065
	$\boldsymbol{\gamma_{max}}$	[10^{-3}]	1.1	1.2	1.2	1.1	1.2	1.1
	$\boldsymbol{W}$	[kips ft]	2.79	92.24	5.03	62.09	23.11	100.63
		[kN m]	*3.78*	*125.06*	*6.82*	*84.18*	*31.33*	*136.44*
4% shear angle	$\boldsymbol{\lambda}$	[ ]	0.67	0.545	0.42	0.34	0.66	0.265
	$\boldsymbol{W}$	[kips ft]	36.52	360.45	51.10	245.18	234.28	421.85
		[kN m]	*49.51*	*488.70*	*69.28*	*332.42*	*317.64*	*571.95*
	$\boldsymbol{W_p}$	[kips ft]	2.43	3.48	1.55	1.70	7.76	1.30
		[kN m]	*3.29*	*4.72*	*2.10*	*2.30*	*10.52*	*1.76*
	$\boldsymbol{W_p/W}$	[%]	6.65	0.96	3.03	0.69	3.31	0.31
	$\boldsymbol{u_{max}}$	[ft]	0.29	1.48	0.65	1.35	2.77	2.46
		[m]	*0.09*	*0.45*	*0.20*	*0.41*	*0.84*	*0.75*

6. Discussion and Final Remarks

The use of topology optimization in the field of diaphragm design, initiated by (Fischer, et al., 2019) and (Fischer, et al., 2020), has been extended to investigation of the capability of traditional and optimized decks to withstand plastic deformation.

The results presented show that, even if the optimized decks were designed to maximize linear elastic stiffness alone, they perform well also in the non-linear regime. In particular, when compared to the traditional designs, the optimized designs:

1. have a higher load carrying capacity, failing at a load that is 19 to 60% higher, for the different diaphragm configurations analyzed;
2. exhibit a stiffer behavior all the way up to the ultimate shear angle;
3. exhibit a much better stress redistribution, resulting in a more dispersed damage pattern, and thus a higher amount of dissipated energy.

This shows the potential for application of topology optimization for the design of innovative deck configurations, even if complicated responses and realistic effects, such as non-linearity, are considered. On the downside, in the optimized decks the yielding happens early, and this may hamper the serviceability of the deck under operational loads. Also, the locations of yielding initialization and the redistribution pattern is somewhat more difficult to foresee for the optimized design than for the traditional one, where the weak spots are easy to locate.

Future development of the work will address the above-mentioned issues. By explicitly accounting for damage in the optimization process, while ensuring that stresses are kept low under service limits, decks can be designed to have maximum stiffness and damage absorption properties. Also, accounting for buckling failure, that is a challenging topic, when coupled with topology optimization (Ferrari & Sigmund, 2019), (Ferrari & Sigmund, 2020), will be a direction of future research. This will help the integration of diaphragm deck design and topology optimization, including stiffness, strength and stability as optimization criteria.

Acknowledgments

The authors gratefully acknowledge the financial support funded by the American Iron and Steel Institute, the American Institute of Steel Construction, the Steel Deck Institute, the Metal Building Manufacturers Association, the Steel Joist Institute and the US National Science Foundation through grant CMMI-1562821. And support from the National Aeronautics and Space Administration (NASA) under Grant No. 80NSSC18K0428. Also, the ideas and contributions from collaborators in the Steel Diaphragm Innovation Initiative (SDII) effort are acknowledged. Any opinions, findings, and conclusions or recommendations expressed in this material are those of the author(s) and do not necessarily reflect the views of the National Science Foundation or other sponsors.

References

AISI, 2013. North American Standard for the Design of Profiled Steel Diaphragm Panels, American Iron and Steel Institute: S310.

ASC, 2018. Composite Deck and Non-Composite Deck for Floor and Roof Deck Applications, s.l.: ASC Steel Deck, v1.0.

ASC, 2018. Roof Deck Design Guide, ASC Steel Deck, v1.0,: s.n.

ASCE 7-16, 2016. Minimum Design Loads and Associated Criteria for Buildings and Other Structures, Reston, Virginia: American Society of Civil Engineers.

Bendsøe, M. P. & Sigmund, O., 2004. Topology Optimization: Theory, Methods and Applications. s.l.: Springer.

Borja, R. I., 2013. Plasticity: Modeling and Computation. s.l.: Springer Verlag.

Deaton, J. D. & Grandhi, R. V., 2014. A survey of structural and multidisciplinary continuum topology optimization: post 2000. Structural and Multidisciplinary Optimization, Volume 49, pp. 1-38.

Easterling, S. et al., 2019. Steel Diaphragm Innovation Initiative. [Online]
Available at: steeli.org

Easterling, S., Sabelli, R. & Sabol, T., 2018. Seismic Design of Composite Steel Deck and Concrete-filled Diaphragms - A Guide for Practicing Engineers, NIST GCR 11-917-10: NEHRP Seismic Design Technical Brief No. 5.

Ferrari, F. & Sigmund, O., 2019. Revisiting topology optimization with buckling constraints. Structural and Multidisciplinary Optimization, Volume 59, pp. 1401-1415.

Ferrari, F. & Sigmund, O., 2020. Towards solving large-scale topology optimization problems with buckling constraints at the cost of linear analyses. Computer Methods in Applied Mechanics and Engineering, Volume 363, p. 112911.

Fischer, A. W., Guest, J. K. & Schafer, B. W., 2019. Novel Building Diaphragm Layouts Generated through Topology Optimization. Nordic Steel.

Fischer, A. W., Guest, J. K. & Schafer, B. W., 2020. Topology Optimization of Cold-Formed Steel Deck Diaphragms with Irregularities. CFSRC Colloquium.

Foroughi, H. et al., 2021. Seismic Behavior of Steel SCBF Buildings Including Consideration of Diaphragm Inelasticity, Baltimore, MD: Cold-Formed Steel Research Consortium Report Series.

Grant, J. & Stewart, S., March 2018. Going with the Flow. AISC Modern Steel Construction, pp. 28-34.

Jones, R., 1999. Mechanics of Composite Materials, 2nd Edition. Philadelphia, PA: Taylor & Francis, Inc..

Luttrell, L., 2015. Diaphragm Design Manual, fourth edition, s.l.: Steel Deck Institute.

Osanov M., G. J., 2016. Topology optimization for architected materials design. Annual Review of Material Research, Volume 46, pp. 211-233.

Schafer, B. W. et al., 2018. Modeling and Performance of Thin-Walled Steel Deck in Roof Diaphragms under Seismic Demands. Lisbon, Portugal, s.n.

Sigmund, O. & Maute, K., 2013. Topology optimization approaches. Structural and Multidisciplinary Optimization, Dec, Volume 48, pp. 1031-1055.

Torabian, S. et al., 2017. SDII Building Archetype Design v1.0, permanent link: jhir.library.jhu.edu/handle/1774.2/4063: CFSRC Report R-2017-04.

Torabian, S., Fratamico, D., Shannahan, K. & Schafer, B., 2018. Cyclic Performance and Behavior Characterization of Steel Deck Sidelap and Framing Connections. 2018 International Specialty Conference on Cold-Formed Steel Structure.

Xia, Y. & Friswell, M., 2012. Equivalent Models of Corrugated Panels, s.l.: International Journal of Solids and Structures, 49, 1453-1462.
Zienckiewicz O. C., T. R. L., 1989. The finite element method: Volume 1. s.l.: McGraw-Hill.

Appendix A

The load increment process with inner iterations through a predictor-corrector material step are the following:

1. Update the load magnitude $F_{ext,k} = \lambda_k F_{ext}$;
2. Initialize displacement to the last converged one $\widetilde{\boldsymbol{u}}_1 = \boldsymbol{u}_{k-1}$
3. While Newton is not converged
    a. Compute $\boldsymbol{\varepsilon} = B\,\widetilde{\boldsymbol{u}}_i$ and $\boldsymbol{\sigma}^{tr} = \boldsymbol{D}^e(\rho_e, \theta_e)\boldsymbol{\varepsilon}$ (elastic predictor)
    b. Identify Gauss points where $\psi(\sigma, \tau_Y) = \psi(\boldsymbol{R}^e(\theta_e)\sigma^{tr}, \tau_Y) \geq 0$ (yielding)
    c. Compute plastic strain and make correction to the stress for Gauss points that are yielding:

$$\dot{\gamma} = \frac{\text{sign}(\tau_0^{tr})|\tau_0^{tr} - \tau_Y|}{H' + G_t'}$$
$$\tau_0 = \tau_0^{tr} - G'\dot{\gamma}$$

    d. Assemble the tangent operator based on the tangent moduli $\boldsymbol{K}_t$
    e. Compute the internal force vector $F_{int,k} = \int_\Omega B^T\,\sigma\ \mathrm{d}\Omega$
    f. Compute the displacements, $\widetilde{\boldsymbol{u}}_{i+1} = \widetilde{\boldsymbol{u}}_i + \delta\widetilde{\boldsymbol{u}}_{\boldsymbol{i}}$, $\delta\widetilde{\boldsymbol{u}}_{\boldsymbol{i}} = K_t(F_{ext,k} - F_{int,k})$
    g. Check convergence
4. Update the yielding stress according to isotropic hardening $\tau_Y = \tau_Y + H'\dot{\gamma}$
5. Set displacement of step *k*: $u_k = \widetilde{\boldsymbol{u}}_{\boldsymbol{i+1}}$
6. Repeat from step 1